The International Journal of Advanced Manufacturing Technology
https://doi.org/10.1007/s00170-026-17780-9

ORIGINAL ARTICLE

Characterisation of infill strategies in WAAM for solid components fabricated with ER100S-G wire

David Gomes Andrade[1] · Carlos Zhu[2] · Hagar El Bamby[3] · Kaike Monteiro[1] · Sree Sabari[1] · Ramesh Babu[4] · Luís Simões da Silva[1] · Trayana Tankova[3]

Received: 23 August 2025 / Accepted: 18 February 2026

Abstract

This study presents a comprehensive characterisation of infill strategies in Wire Arc Additive Manufacturing for the fabrication of thick-walled steel components using ER100S-G wire. The primary objective of this work is to systematically assess how different combinations of edge and infill deposition strategies influence the thermal behaviour, defect formation, surface quality, and resulting microstructural and mechanical properties of solid WAAM components. Eleven deposition strategies, combining edge and infill parameters under two heat input configurations, were systematically evaluated. Thermal analysis based on Δt_{8-5} cooling times revealed significant heat accumulation in corner regions and extended deposition paths, with cooling times increasing by up to approximately threefold depending on the deposition strategy and location. Microstructural characterisation identified acicular ferrite and bainite with refined grains in faster cooling zones. Electron Backscatter Diffraction confirmed grain growth and local misorientation reduction with increased heat input, alongside a transition from low-angle to high-angle grain boundaries, indicating partial recrystallisation and microstructural recovery. Laser profilometry showed that surface height variation remained below 1 mm in all samples, yet concentric infill strategies and non-weaving conditions resulted in the most irregular surfaces, affecting dimensional precision and post-processing requirements. Defects such as pores, lack of fusion, and overlaps were more frequent in low-energy or non-weaving strategies due to poor material distribution. Finally, hardness measurements confirmed that faster cooling rates ($\Delta t_{8-5} < 12$ s) led to higher hardness values, reinforcing the relationship between thermal history and mechanical response.

Overall, the results demonstrate that infill strategy selection plays a critical role in balancing productivity, thermal stability, surface quality, and structural integrity in WAAM-fabricated solid components. These findings offer valuable insights into the process–structure–property relationships in WAAM, providing practical guidance for optimising the production of defect-minimised and structurally consistent solid steel components.

Keywords WAAM · Infill Strategies · ER100S-G Steel · Microstructural Analysis · Mechanical Properties

1 Introduction

Wire Arc Additive Manufacturing (WAAM) is a Directed Energy Deposition (DED) process within Additive Manufacturing (AM) technologies, known for its capability to produce large-scale metallic components with high deposition rates and near-net-shape geometries. Unlike powder-based AM techniques such as Selective Laser Melting (SLM), WAAM enables the production of large and fully dense components, which is advantageous for improving both static performance and fatigue life [1]. Moreover, WAAM allows for better control of mechanical properties in thick components by locally adjusting processing parameters, a

✉ Trayana Tankova
t.tankova@tudelft.nl

[1] Department of Civil Engineering, University of Coimbra, ISISE, ARISE, Coimbra, Portugal

[2] Department of Mechanical Engineering, University of Coimbra, CEMMPRE, ARISE, Coimbra, Portugal

[3] Department of Engineering Structures, Delft University of Technology, Delft, the Netherlands

[4] DNV, Hovik, Norway &LNU, Sweden

Published online: 26 February 2026

capability that addresses limitations observed in hot-rolled plates, where mechanical properties typically degrade with increasing thickness [2]. These qualities make WAAM an attractive technology for industrial applications [3–5]. However, its widespread adoption remains limited due to property variations arising from layer-by-layer thermal fluctuations, which are strongly influenced by deposition strategies in multi-bead builds, particularly in thick-walled components where infill sequence and pattern play a critical role.

In this context, few studies investigated the influence of printing strategies on the resulting microstructure, grain orientation and mechanical anisotropy of thick WAAM components. For example, the study in [6] provided a detailed analysis of the microstructural characteristics of multi-walled thick structures produced using 316LSi. The study observed that the microstructure of the fusion zone was influenced by uneven layer heights, which increased the contact-tip working distance and wire resistance. Similarly, in [7] the microstructure of multi-walled thick walls produced from 316LSi was analysed. The components studied exhibited periodic microstructural changes based on the deposition strategy used. In the transverse direction, two alternating microstructures were observed, the re-melting and the overlapping areas. In the re-melting area, the grains grew perpendicular to the fusion lines, while in the overlapping regions, the grains grew along the building direction. Several authors have linked this periodic heterogeneous microstructure to the anisotropic uniaxial tensile behaviour of thick components produced by WAAM in 316 L steels [8, 9] and carbon steel [10, 11].

To build thick components, the infill pattern can typically be divided into linear path planning, contour path planning, and a hybrid approach that integrates both strategies [12–15]. The influence of slicing strategies on the microstructure of multi-walled thick walls produced in 316LSi was further explored in [16]. This study evaluated three deposition paths: layer-wise unidirectional, layer-wise weaving, and bidirectional zigzag scanning. Among these, the bidirectional zigzag strategy produced a more homogeneous microstructure, significantly improving isotropic mechanical properties. More recently [17], also investigated the influence of various tool path trajectories, including spiral and zigzag, on the fabrication of bulk NiCrMo components. Their findings confirmed that the chosen trajectory directly dictates microstructural heterogeneity and the anisotropic mechanical response of the solid, reinforcing the need for strategy-specific characterisation.

Since the metallic parts are fabricated based on a layer-by-layer principle, the interactions between the neighbouring beads and layers strongly influence the geometric accuracy of the fabricated part [18]. In this context, in [19] various infill patterns were compared and it was noted that zigzag patterns, where the welding direction reverses by 180°, often lead to material accumulation at turning points with weld defects or lack of fusion along the outer radius. Similarly, spiral patterns exhibited material buildup as the radius decreased toward the centre, resulting in an uneven deposition.

Accurate modelling of weld bead geometry and overlapping paths is also essential for ensuring dimensional accuracy and surface quality in WAAM components [20–24]. Various models have been proposed to predict the optimal centre distance between adjacent beads, such as the flat-top and tangent overlapping models, which account for bead shape and spreading effects [22, 23]. Similarly [25], demonstrated through Response Surface Methodology that optimising the layer-stacking sequence is critical for controlling bead morphology and hardness distribution. Also, recent advances in path planning have further addressed these challenges, where [26] developed continuous printing path algorithms specifically designed to maintain connectivity and control density in complex infills. While these models provide valuable guidelines for process planning, they often rely on simplified assumptions, such as constant deposition parameters or idealised heat transfer conditions, that do not fully capture the complexities encountered in fabricating thick-walled components. Moreover, most modelling approaches focus on bead-level geometry optimisation, leaving the combined effects of edge and infill strategies, thermal accumulation, and practical build efficiency largely unaddressed. In particular, the influence of strategy combinations, such as alternating deposition directions, weaving, or overlap configurations, on the thermal history, microstructure, and defect formation remains insufficiently explored through experimental studies.

For thick components with overlapping weld beads, the thermal cycles are also significantly more complex than those in thin walls due to the three-dimensional heat dissipation and the intricate interactions between adjacent beads. The impact of various infill strategies on the temperature field and residual stresses in Al-4046 material was analysed in [27]. Their findings revealed that the “S” pattern produced a more uniform temperature distribution, leading to improved microstructure, reduced porosity, and minimised residual stress compared to meander and spiral patterns.

Although significant advancements have been made in WAAM research to produce thick components, there is a notable gap in the systematic analysis of infill printing strategies and their effects on critical parameters such as thermal cycles, microstructural evolution, production rates, and defect formation. Most existing studies focus on isolated strategies or limited parameter sets, leaving the combined influence of edge and infill strategies underexplored. While

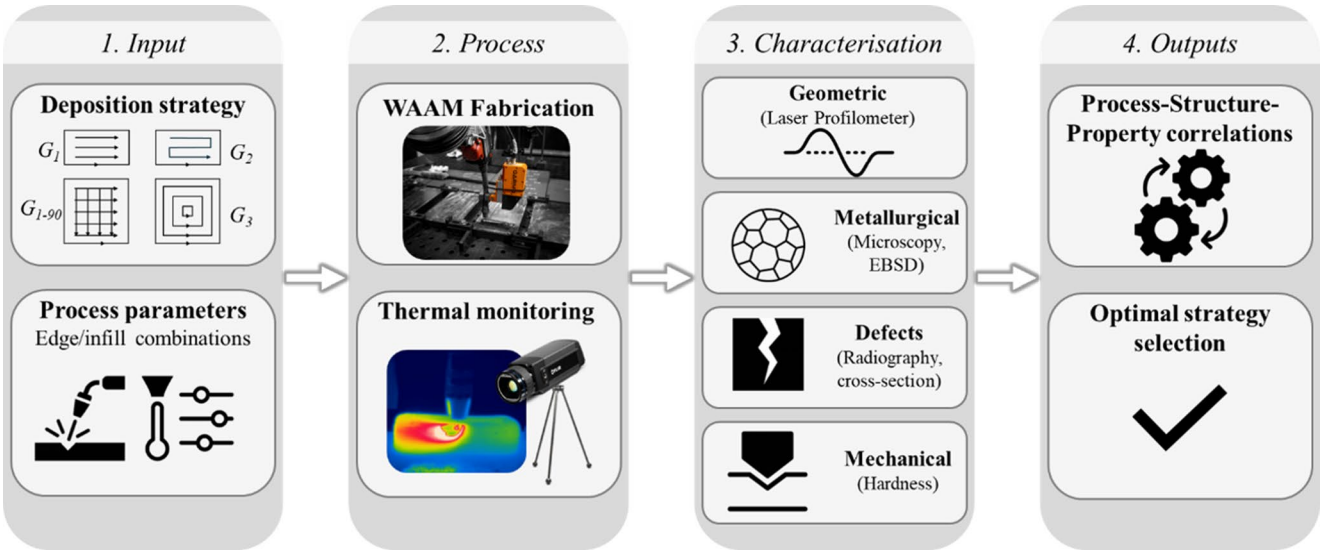

Fig. 1 Schematic overview of the experimental workflow and intent of the study

Table 1 Chemical composition and mechanical properties of the as-deposited material (ER100S-G steel)

Wire	Chemical composition (wt %)							Mechanical Properties		
	C	Si	Mn	Cr	Ni	Mo	Fe	Yield strength [MPa]	Tensile strength [MPa]	Elongation [%]
ER100S-G	0.08	0.60	1.70	0.20	1.5	0.50	Bal.	720	780	16

recent work by [28] has established robust process windows and mechanical correlations for steel WAAM walls under various transfer modes, a systematic analysis of infill strategies for solid components remains limited. This lack of comprehensive analysis limits the potential to optimise WAAM for producing thick-walled components with consistent mechanical properties, dimensional control and minimal defects.

This study addresses these gaps by investigating eleven infill strategies under varied processing conditions. Two combinations of edge and infill strategies were tested, employing different heat inputs to fabricate rectangular and square samples. As schematically illustrated in Fig. 1, the experimental framework is structured around four main stages: input definition, WAAM processing, multi-scale characterisation, and output evaluation. The inputs comprise the selection of deposition strategies and process parameter combinations for edge and infill regions, followed by WAAM fabrication under controlled conditions. During processing, a thermographic camera was used to monitor thermal cycles and inter-pass temperatures, enabling a direct assessment of heat accumulation effects. The fabricated components were subsequently characterised using complementary techniques, including microstructural analyses to correlate thermal history with printing strategies, Electron Backscatter Diffraction (EBSD) to analyse crystallographic orientation, and X-ray inspections for defect detection. Surface morphologies were assessed using laser profilometry to quantify waviness and evaluate dimensional consistency across strategies, while hardness measurements were performed to assess local mechanical responses within the component volume and between edge and infill regions. Finally, the combined results enable the establishment of process–structure–property relationships and support the identification of optimal infill and edge deposition strategies for thick-walled WAAM steel components.

2 Materials and methods

2.1 Experimental setup and deposition strategies

2.1.1 Materials and manufacturing system

The thick-walled solids were fabricated using an ABB IRB 4600 robot and a Fronius TPS 400i Cold Metal Transfer (CMT) welding machine. The feedstock material used for WAAM printing was ER100S-G (AM 70) steel wire supplied by Voestalpine Böhler Welding, with a diameter of 1.2 mm. The mechanical properties and chemical composition of the as-deposited feedstock material, as provided by the manufacturer, are detailed in Table 1. To ensure compatibility with the welding wire, M21 shielding gas, with a mixture of 82% Argon and 18% CO_2, was used at a flow rate of 20 L per minute. The substrate used in this study matched the feedstock material chemical and mechanical properties.

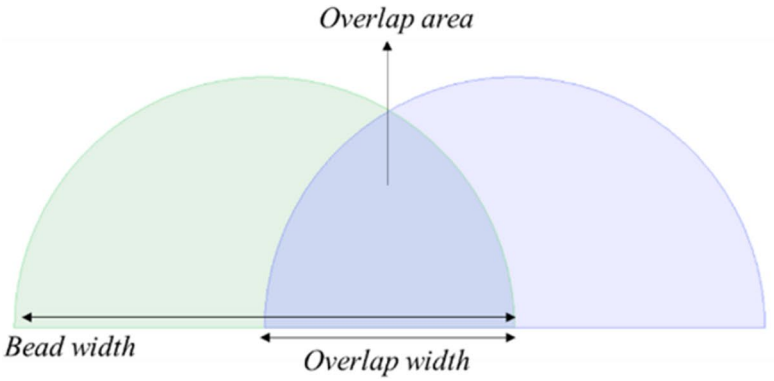

$$Overlap\ Percentage = \frac{Overlap\ width}{Bead\ width} \times 100$$

Fig. 2 Schematic representation of the calculation of the overlap percentage

Specifically, 40 mm thick steel plates of grade S690QL, according to the specifications outlined in EN 10025-6:2019 [29], were selected.

2.1.2 Deposition strategies and process parameters

A thick solid comprises multiple overlapping beads, following a similar convention adopted by [6], and not a single weld pass that produces a thick component [30]. The solid contains two types of weld beads, namely edge and infill beads. The edge bead functions as the contour of the geometry and the infill forms the inner volume. In these strategies, the critical scenarios for the interaction between beads are identified, namely (1) the overlap of dissimilar weld beads (edge-infill), and (2) the overlap of infill beads (infill-infill). The definition of bead overlap adopted in this study is schematically illustrated in Fig. 2. The overlap ratio was defined as the ratio between the overlap width of two adjacent beads and the nominal bead width, based on the effective bead geometry measured from single-layer depositions. In preliminary studies, overlap ratios between 60% and 70% were found to be optimal for achieving flatter surface profiles, consistent with findings reported in the literature [24, 31].

In this study, deposition strategies and combinations of edge and infill deposition parameters are tested. For each sample, different process parameters were tested for the infill and edge depositions. Namely, two configurations, combination 1 and combination 2, were tested to characterise deposition conditions with high and low heat input. Specifically, the 150 A, 2.5 mm/s edge parameter was combined with the 240 A, 7.5 mm/s infill parameter. On the other hand, the 60 A, 3 mm/s edge parameter was combined with the 150 A, 5 mm/s infill parameter. The heat input and deposition rates of the process parameters are summarised in Table 2. The heat input (HI) was calculated according to [32] using the following relationship:

Table 2 Deposition parameters: combinations between edge and infill parameters

Parameter		Current [A]	Travel speed [mm/s]	Heat input [kJ/mm]
Combination 1	**Edge 1**	150	2.5	1.3
	Infill 1	240	7.5	0.8
Combination 2	**Edge 2**	60	3	0.4
	Infill 2	150	5	0.6

$$HI = \frac{Current \times Voltage}{Travel\ speed} \quad (1)$$

The selection of parameters was tailored to optimise different aspects of the deposition process. For the edge passes, conditions were chosen to enhance surface finish and dimensional accuracy, whereas for the infill, parameters were selected to maximise deposition rate. In combination 1, the edge deposition featured a higher heat input compared to the infill, while in combination 2, the infill exhibited a higher heat input relative to the edge.

The tested deposition strategies are denoted as G1, G1-90, G2, and G3, and are schematically represented in Fig. 3. In this figure, orange beads denote the infill deposition, yellow beads denote the edge deposition, the green and red points represent the start and stop positions of each weld bead and the black arrows indicate the trajectory of the deposition torch. Figure 3 also illustrates the management of starting and ending points between consecutive layers (Layer n and Layer $n+1$) to demonstrate the alternation logic used to mitigate local heat accumulation.

A description of the deposition strategies is provided in the bullet points below:

- G1 strategy employs an infill pattern consisting of parallel deposition lines, with the start and end points alternating between layers to achieve a more even heat distribution.

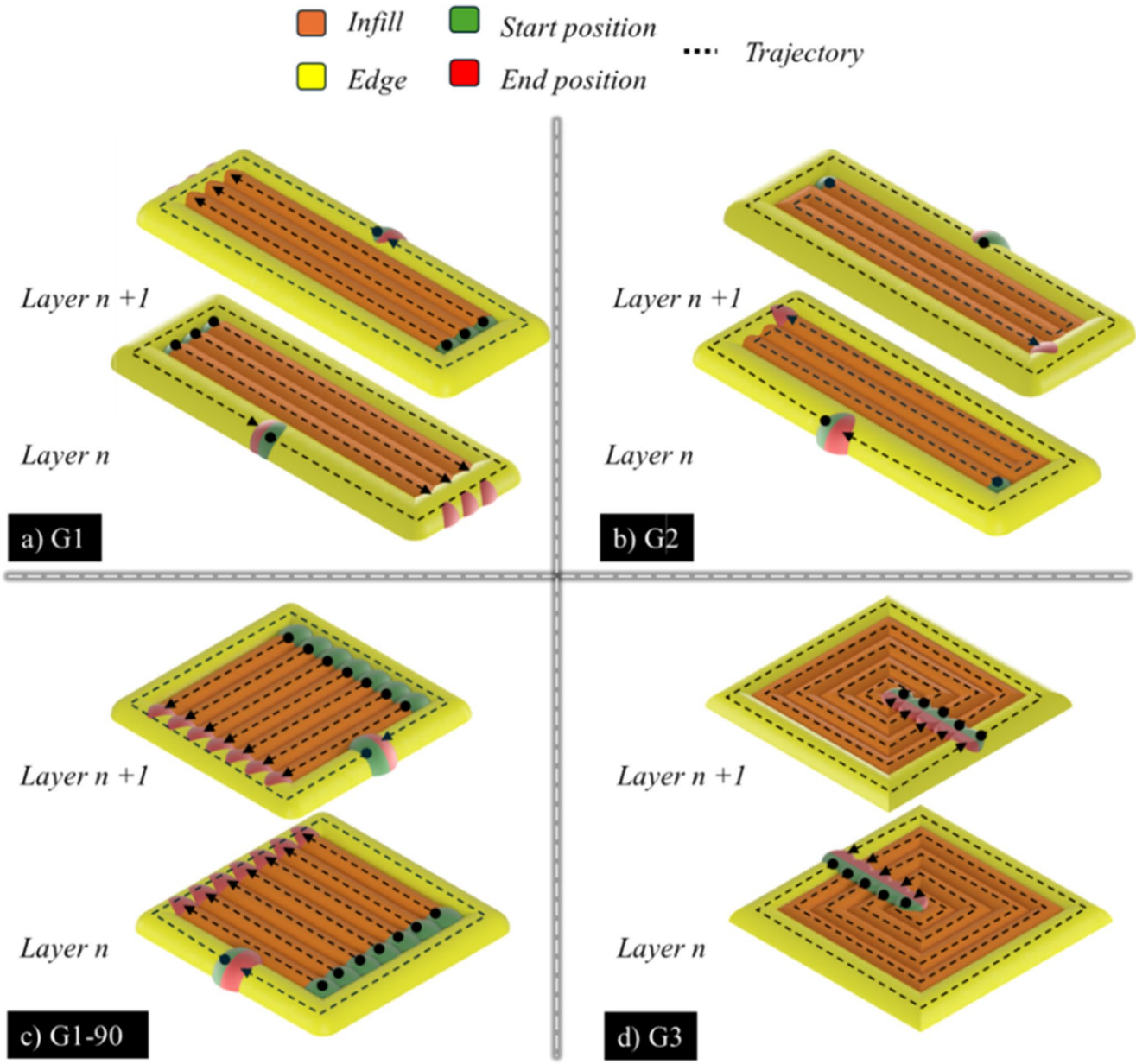

Fig. 3 Schematic representation of the deposition strategy sequences: (**a**) G1, (**b**) G2, (**c**) G1-90 and (**d**) G3

- G1-90 strategy is similar to G1 but introduces a 90º shift in the deposition orientation between consecutive layers while maintaining alternating start and stop positions.
- G2 strategy uses a single deposition line for the infill, with alternating start and stop positions across layers to ensure even heat dissipation.
- G3 strategy represents concentric pattern, alternating between clockwise and counterclockwise orientations for each successive layer.

The G1 and G2 strategies were implemented using a rectangular cross-section with dimensions of 100 × 50 mm, as they focus on directional deposition patterns more suitable for elongated geometries. The G1-90 and G3 strategies were produced with a square cross-section measuring 100 × 100 mm, as they are doubly symmetric and are more effectively tested on symmetric geometries. Each component was fabricated with a total of eight layers, which allowed for sufficient build height to observe the transition in thermal cycles and microstructural features across layers.

In addition, two weaving conditions were tested for the infill. The first condition involved no weaving, while the second applied a weaving amplitude of 3 mm with a frequency of 1 Hz in a Zigzag pattern. Different deposition sequences were tested to assess their influence on the component quality, in this case using two distinct approaches

Table 3 WAAM printing strategy

Sample ID	Nomenclature	Deposition parameters	Type	Weaving Amplitude	Overlap Edge-Infill	Overlap Infill-infill	Sequence
S1	G1_C1_W_60_FE	Combination 1	G1	3	60%	70%	Infill-Edge
S2	G1_C1_N_60_FE	Combination 1	G1	None	60%	70%	Infill-Edge
S3	G1_C1_W_70_FE	Combination 1	G1	3	70%	70%	Infill-Edge
S4	G1_C1_W_60_EF	Combination 1	G1	3	60%	70%	Edge-Infill
S5	G1-90_C1_W_60_FE	Combination 1	G1-90	3	60%	70%	Infill-Edge
S6	G2_C1_W_60_FE	Combination 1	G2	3	60%	70%	Infill-Edge
S7	G3_C1_W_60_EF	Combination 1	G3	3	60%	70%	Edge-Infill
S8	G3_C1_N_60_EF	Combination 1	G3	None	60%	70%	Edge-Infill
S9	G1_C2_W_60_FE	Combination 2	G1	3	60%	60%	Infill-Edge
S10	G2_C2_W_60_FE	Combination 2	G2	3	60%	60%	Infill-Edge
S11	G3_C2_W_60_EF	Combination 2	G3	3	60%	60%	Edge-Infill

where the infill was printed first and then followed by the edge, and another approach where the edge was printed first and then followed by the infill. By varying the deposition trajectories and orientations, this study provides insights into how different strategies influence the quality and structural integrity of WAAM components.

The parameters used to produce the thick-walled components are summarised in Table 3. Table 3 is organised to facilitate a clear understanding of the parameters studied and the variations between the different samples. The nomenclature used in the table provides an identification of each sample by encoding the deposition strategy, parameter combination, weaving condition, overlap percentage, and sequence type. For instance, the nomenclature G1_C1_W_60_FE represents the solid sample S1, produced with the G1 deposition strategy, combination 1 parameters (Table 2), a weaving amplitude of 3 mm (indicated by "W"), a 60% overlap between the edge and infill, and an Infill-Edge sequence. For example, solid S2, identified as G1_C1_N_60_FE, was produced with the same parameters as S1 but without weaving (indicated by "N"). Also, solid S1 is referred to as the reference component since all other tests were conducted by modifying one or more of these process parameters to evaluate their effects on the deposition process and component quality.

2.1.3 Process monitoring

In all cases, the inter-pass temperature and the temperature between beads were set to a maximum of 250 °C. The inter-pass temperature and the deposition thermal cycles were monitored using a FLIR A655sc thermographic camera with a sensor resolution of 640 × 480 pixels, following the procedures and recommendations outlined in [33]. The camera was mounted at a distance of approximately 500 mm from the substrate, capturing a field of view of 415 mm width. This setup resulted in a spatial resolution of approximately 0.65 mm per pixel. The system operates with a measurement accuracy of 2% of the reading and a thermal sensitivity of 0.03 °C. Data was acquired at a frame rate of 25 Hz. The surface emissivity of the WAAM steel component was calibrated to a value of 0.65 using a K-type thermocouple as a reference.

After the deposition of each layer, a Garmo Garline laser profilometer, mounted on the robotic arm system, was used to acquire surface morphology data. The sensor operates with a lateral resolution of ± 0.03 mm and a depth resolution of ± 0.07 mm. The surface scans were conducted with a travel velocity of 10 mm/s and an acquisition frame rate of 25 frames per second. These measurements enabled the monitoring of layer waviness and surface profile evolution throughout the build following the procedures outlined in [34]. The complete experimental setup, highlighting the integration of the monitoring systems, is shown in Fig. 4.

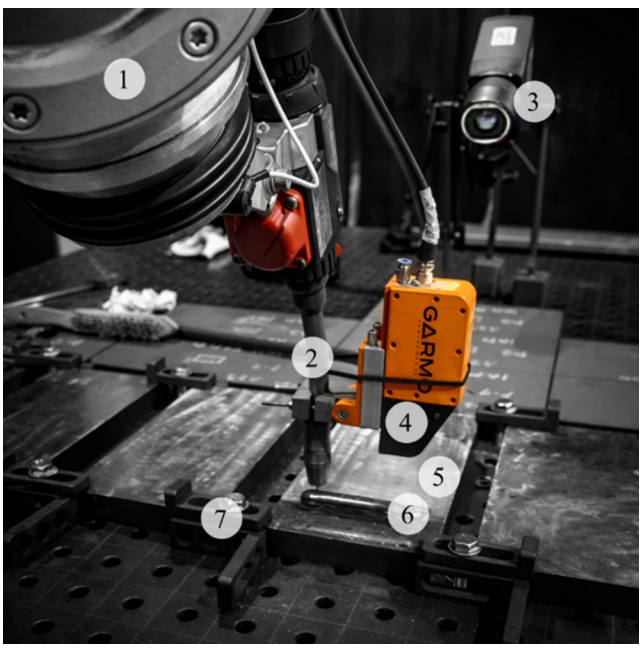

Fig. 4 Experimental setup used for the WAAM fabrication and monitoring: (1) robotic arm, (2) WAAM torch, (3) thermographic camera, (4) laser profilometer, (5) substrate, (6) WAAM part and (7) clamping system

2.2 Material characterisation and analysis

Macro sections with a thickness of 15 mm, including the substrate and the printed solid, were extracted in the transverse direction from the middle and corner regions of the components, as illustrated in Fig. 5, to investigate the geometric and metallurgical characteristics of the produced solids. The extracted samples were mounted in resin to facilitate easier handling during subsequent preparation and analysis. Sample preparation followed the procedures outlined in ASTM E3-01 [35]. After etching with 2% Nital, a metallurgical analysis was conducted using an optical digital microscope. This analysis aimed to identify variations in the microstructure, delineate the boundaries of the weld, heat-affected zone, and base material, and detect flaws or inclusions within the samples. To further analyse the microstructural evolution and crystallographic features of the deposited material, EBSD was also performed.

To detect macroscopic porosities and internal defects, radiographic testing was performed with Iridium-192 source in accordance with EN ISO 17636-1:2022 [36]. The location of the samples extracted for the radiographic testing is also shown in Fig. 5. Both the radiographic and metallographic samples were taken from a plane intersecting the start and end positions of the depositions, as these regions are more susceptible to defect formation. All tests were conducted 72 h after the walls were fabricated.

To complement these analyses and investigate the influence of different printing strategies on the mechanical properties of the components, Vickers microhardness measurements were performed on the cross-sections of the metallographic samples. The hardness tests were conducted using a load of 500 g, a holding time of 15 s, and a spacing of 0.5 mm between indentations.

3 Results and discussion

3.1 Thermal analysis of deposition cycles

Figure 6a represents the methodology used to acquire thermal cycle data, showing a thermographic image of the heat distribution during deposition for the reference sample G1_C1_W_60_FE (sample S1, as detailed in Table 3). Multiple measurement points were placed approximately every 10 mm along the deposition line to capture spatial variations in thermal behaviour. For each deposited sample, one thermal cycle was recorded at each measurement point during the deposition process. Figure 6b shows the spatial distribution of the cooling times between 800 °C and 500 °C (Δt_{8-5}) across the eighth and final layer being deposited, reflecting the thermal behaviour closer to steady-state conditions. The Δt_{8-5} parameter was selected as the primary thermal descriptor because this temperature interval governs the solid-state phase transformation of austenite in low-alloy steels and allows a direct correlation between thermal history, microstructural evolution, and resulting hardness [37]. The values obtained from the measurement points are represented as circles, with a colour map indicating the corresponding Δt_{8-5}. These points include infill and edge depositions, ensuring comprehensive coverage of the thermal cycle data across the component. Additionally, Fig. 6c shows the evolution of the Δt_{8-5} with layer height at several critical locations, such as infill (black dot), edge corner (red dot), start (green dot) and end positions (yellow dot).

The analysis of the Δt_{8-5} spatial distribution for the last layer being deposited reveals variations ranging from 9 to 63 s. The infill regions exhibited shorter cooling times compared to the edges, which can be attributed to the lower heat input of the infill, despite the higher current used for these depositions, as shown in Table 2. This difference is also explained by the more consistent heat transfer within

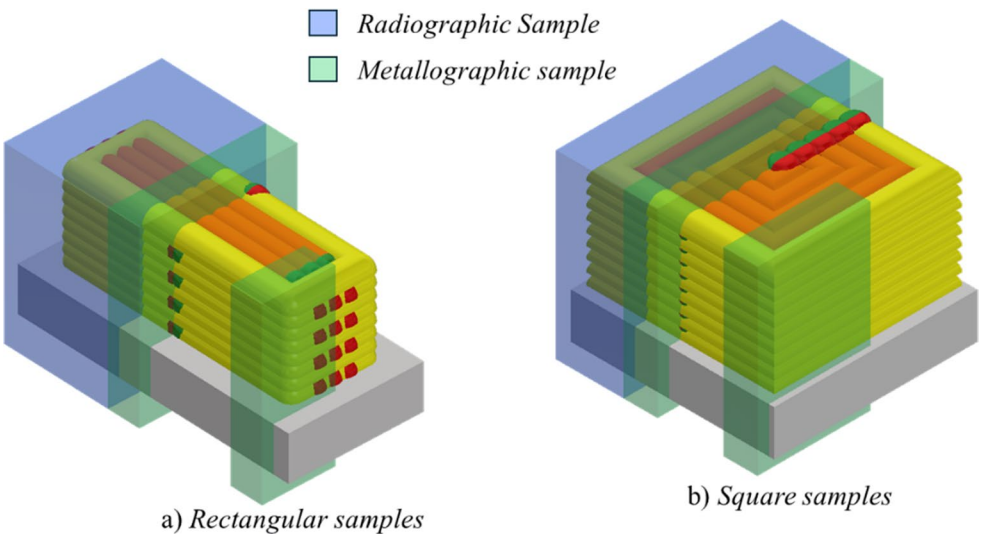

Fig. 5 Schematic representation of the extraction zones for the metallographic and radiographic samples for the (**a**) rectangular and (**b**) square geometries

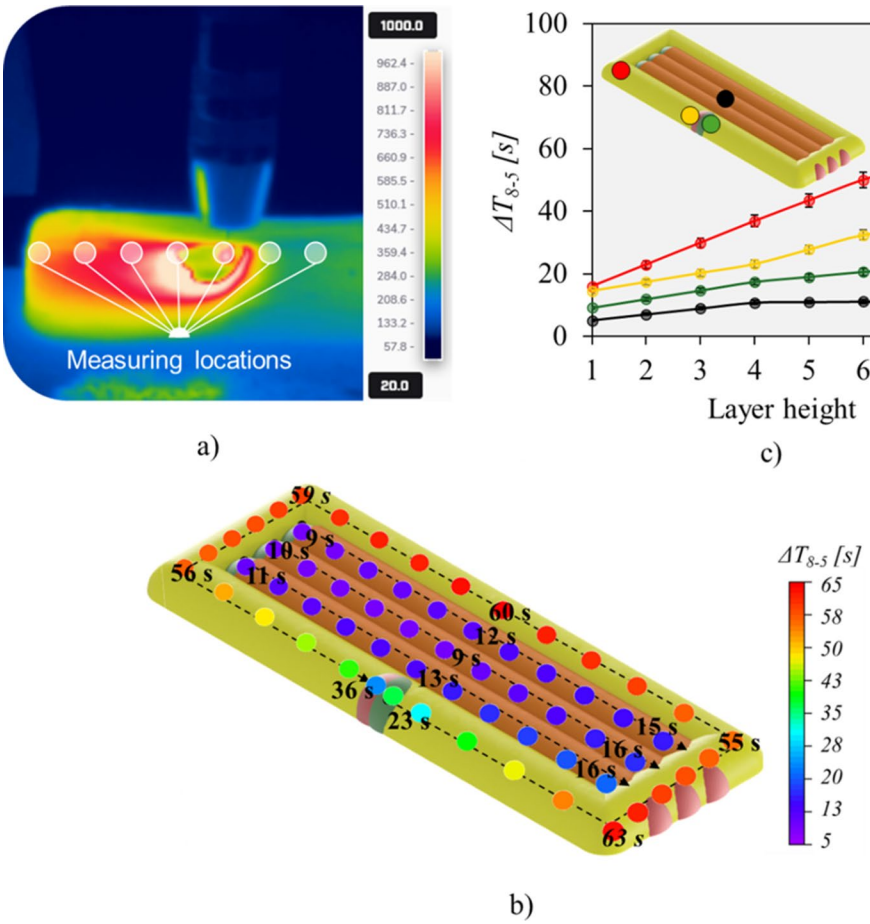

Fig. 6 (**a**)Thermographic image illustrating the measurement points positioned along the deposition line, used for the thermal cycle analysis of the reference sample G1_C1_W_60_FE (S1). (**b**) Spatial distribution of $\Delta t_{8\text{-}5}$ cooling times across the eighth layer. (**c**) Evolution of $\Delta t_{8\text{-}5}$ cooling times with layer height at selected locations. Error bars represent the measurement uncertainty associated with the thermographic system accuracy

the infill regions, where neighbouring material facilitates heat dissipation. In contrast, since the edges were produced with a higher heat input deposition parameter and are more exposed to open air, they experience reduced heat dissipation and longer cooling times.

Typically, the start positions for both the edge and infill depositions showed shorter cooling times due to lower heat accumulation at the beginning of the deposition process. As the deposition progresses, the cooling times tend to increase, reflecting the accumulation of heat within the volume. In addition, the final deposition positions exhibited the longest cooling times because the deposition torch was kept stationary at these locations, for 1 s before arc extinction, to deposit additional material and prevent the typical sloping of material often observed at the termination points.

For longer deposition runs, such as the edge depositions where the full contour of the solid was completed, the cooling rates slightly decreased toward the end of the path, despite the 1-second torch pause immediately before arc extinction. This was due to the cessation of the heat source, which reduced the overall heat. This effect was evident after the deposition of the last corner, where the cooling times decreased from 56 to 36 s.

Lastly, by analysing Fig. 6c, it is possible to observe a clear upward trend in Δt_{8-5} cooling times with increasing build height across all monitored positions, indicating progressive thermal accumulation. This effect is most pronounced in the edge corner region (red point), where Δt_{8-5} rises from approximately 16 s in the first layer to over 60 s in the eighth. In contrast, the infill region exhibits a more stable thermal behaviour, maintaining relatively consistent cooling times, which suggests more effective and uniform heat dissipation as the build progresses. These results highlight the limitations of relying solely on a fixed inter-pass temperature to regulate thermal cycles in thick-walled components. Although a global inter-pass temperature of 250 °C was strictly maintained, it failed to prevent progressive heat accumulation in strategies with high duty cycles. This demonstrates that the deposition strategy acts as a dominant thermal regulator, capable of overriding the effects of the inter-pass temperature control. Therefore, optimising thermal cycles for multi-pass deposition requires strategy-specific path planning to mitigate local saturation, rather than reliance on global temperature thresholds alone.

Furthermore, although only one trial per strategy was performed, the observed differences in Δt_{8-5} cooling times between deposition locations, such as the pronounced

differences between corners and straight deposition paths, as well as their evolution with build height, are considered substantial and reproducible. These deviations far exceed the temporal and thermal resolution of the monitoring system (Sect. 2.1.3), confirming that they reflect systematic, strategy-dependent heat accumulation effects rather than random measurement variability or equipment noise.

Figure 7 shows the Δt_{8-5} cooling times for all samples analysed in this study, measured at representative locations within the infill and edge regions of each component. For the infill, Δt_{8-5} values were recorded at the midpoint of the deposition path (black point, as indicated in Fig. 6c), whereas for the edge, measurements were taken at the end position of the contour pass (yellow point, as indicated in Fig. 6c). All measurements were taken from the eighth and final deposited layer, representing thermal conditions closer to steady state.

The results reveal significant variations in the Δt_{8-5} cooling times across the different deposition strategies and process parameters for both infill and edge regions. For the samples produced using combination 1 (S1 to S8), the Δt_{8-5} cooling times in the infill region were consistently smaller than those observed in the edge region. In contrast, for the samples produced using combination 2 (S9 to S11), the cooling times in the infill region were always longer than those at the edge. This difference is primarily attributed to the heat input associated with the selected parameters.

The influence of weaving can be assessed by comparing S1 with S2 and S7 with S8 samples. The results indicate that the absence of weaving had an insignificant impact on the cooling times, suggesting that this parameter does not play a major role in heat dissipation within the conditions tested. Similarly, variations in overlap percentage within the range explored in this study also showed negligible effects on Δt_{8-5}, as observed by comparing S1 with S3 samples. On the other hand, the order in which the printing occurred, specifically whether the infill or edge was deposited first, had a more pronounced effect on the cooling behaviour of the edge bead. For sample S4, where the edge was deposited first, the Δt_{8-5} cooling times in the edge region were shorter compared to the reference sample (S1), where the infill was deposited first. This suggests that depositing the edge first may facilitate faster cooling by allowing the edge material to dissipate heat without the influence of prior infill deposition. However, the infill cooling times in sample S4 were similar to those in S1, indicating that the deposition sequence had small impact on the infill region.

The different deposition strategies, G1-90, G2, and G3 presented distinct thermal cycles. The G1-90 strategy did not significantly change the cooling times for the edge or infill regions. The G2 strategy exhibited the highest cooling times for the infill regions among all samples, attributed to the continuous infill deposition pattern. The lack of stops concentrates heat along the trajectory, leading to significant heat accumulation and slower cooling. In contrast, the G3 strategy demonstrated faster cooling rates for the edge regions, as the edge was deposited first, allowing faster heat dissipation. However, the infill region showed higher cooling times due to the concentric deposition pattern, which requires longer deposition time for each pass of the infill.

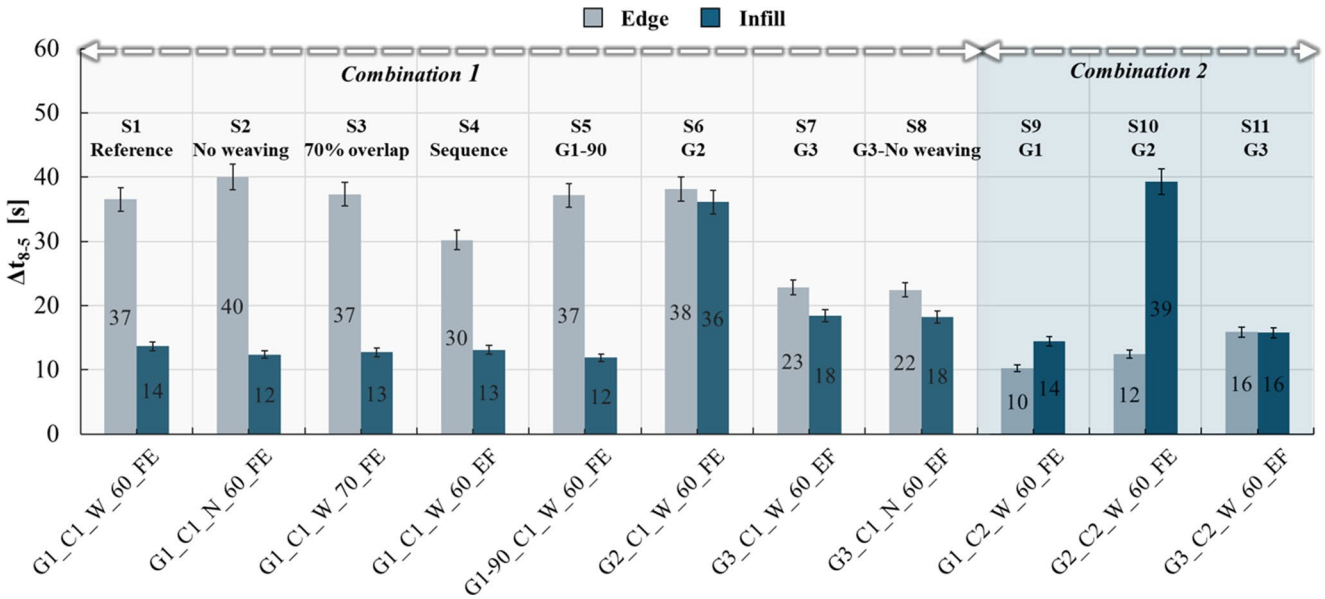

Fig. 7 Δt_{8-5} cooling times measured for all samples in the infill (at 50% of the total deposition length for the last infill bead deposited) and the edge (at the deposition ending position) locations. Each sample is identified by its nomenclature, with the main parameter variations highlighted for comparison against the reference sample (S1). Error bars represent the measurement uncertainty associated with the thermographic system accuracy

Table 4 Influence of process parameters on cooling time $\Delta t_{8\text{-}5}$

Process variable	Physical explanation
Layer height	Significant increase in cooling time due to progressive heat accumulation in the component volume as distance from the substrate increases.
Deposition location	Corners experience the highest cooling times due to heat saturation from converging deposition paths.
Weaving	The presence or absence of weaving does not significantly modify heat dissipation under the investigated conditions.
Overlap percentage	Variations in overlap within the tested range do not significantly affect thermal dissipation or heat accumulation.
Deposition sequence	Depositing the edge prior to the infill promotes faster cooling of the edge bead, as heat is dissipated directly to the surrounding air without the thermal buffering effect of a pre-existing infill.
Infill strategy	Both strategies led to increased cooling times compared to discontinuous paths. G2 removes arc-extinction pauses, leading to maximum heat concentration, while the inward spiral of G3 forces the arc to deposit into an increasingly heated centre.
Heat input	Direct correlation where lower heat input consistently resulted in the shortest cooling times, regardless of strategy.

This prolonged deposition duration contributes to localised heat accumulation, slowing the cooling cycle. It is important to note that the influence of the G1-90, G2, and G3 on the deposition thermal cycles was consistent across both combination 1 and combination 2.

To summarise the thermal analysis, Table 4 presents a synthesis of the influence of the different process parameters and deposition strategies on the cooling time Δt_{8-5}, along with the physical mechanisms governing these effects.

3.2 Morphological characterisation

In this section, a comprehensive analysis of the morphological features of the fabricated samples is presented. This includes an evaluation of the bead geometry, layer stacking morphology, and the homogeneity of the deposited material. Figure 8 illustrates the geometry of the components produced with rectangular sections (samples S1, S6, and S9) and square sections (samples S5 and S11), providing examples of the effect of different deposition strategies and parameters on the final geometry. All samples successfully achieved the intended rectangular or square cross-sections, demonstrating the reliability and adaptability of the WAAM process in fabricating solid thick components with varying shapes. The inherent surface waviness characteristic of WAAM is evident in all samples, particularly along the top layers and edges. This waviness results from the layer-by-layer deposition process and can be attributed to bead stacking and the thermal gradients present during fabrication.

To quantitatively assess the surface morphology of the first deposited layer across all WAAM strategies, laser profilometry scans were performed, as presented in Fig. 9. Figure 9a shows the 3D surface scans for each sample, with

Fig. 8 Geometry of WAAM-fabricated components with rectangular (S1, S6, S9 samples) and square (S5, S11 samples) sections

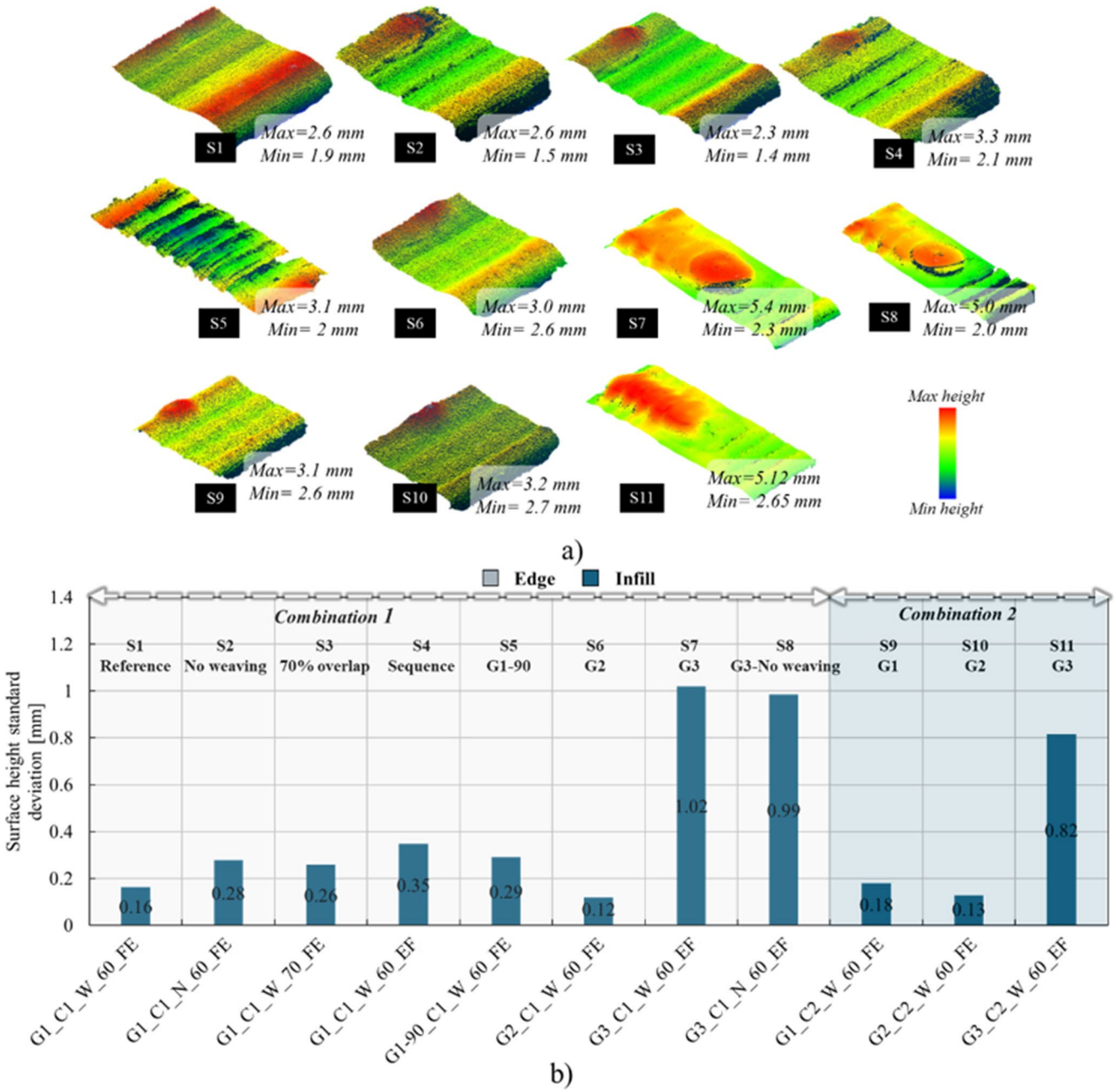

Fig. 9 Laser profilometry results for the first layer of each WAAM-fabricated component: (**a**) 3D surface scans with colour maps representing relative height and (**b**) chart with the standard deviation of height values within the infill region

colour-coded height maps indicating relative elevation, where blue regions represent lower surface areas and red regions correspond to raised peaks. For each sample, the colour scale is normalised so that the minimum and maximum colours correspond to the lowest and highest measured surface heights, respectively, with the corresponding height values explicitly indicated. In parallel, a quantitative evaluation of surface flatness was carried out by calculating the standard deviation of surface height within the infill region, as illustrated in Fig. 9b.

Among the samples produced using Combination 1, sample S6 (G2 strategy) exhibited the lowest standard deviation (0.12 mm), corresponding to the flattest surface. This result is attributed to the continuous linear deposition path, which promotes consistent bead stacking. In contrast, samples S7 and S8 (G3 strategy, with and without weaving, respectively) displayed the highest surface variability (1.02 mm and 0.99 mm), evidencing pronounced waviness induced by the concentric deposition pattern and heat accumulation. This effect is further amplified by the fact that the

start and stop positions in the G3 strategy are concentric and located near the centre of the part, leading to material build-up. In Combination 2, the influence of deposition strategy remained similar. Sample S10 (G2) maintained a low surface roughness (0.13 mm), whereas S11 (G3) exhibited a high deviation (0.82 mm), although slightly improved compared to Combination 1 due to the lower heat input used.

Within the G1 infill strategy, namely S1, S2, S3, S4, and S5 samples, which share the same path but differ in process variations such as weaving, overlap percentage and deposition sequence, the standard deviation values ranged from 0.16 mm to 0.35 mm, indicating that even minor changes in process parameters have a measurable impact on surface flatness. Comparing S1 and S2, the absence of weaving increased surface waviness, confirming the role of weaving in promoting more homogeneous material distribution and surface smoothing. Similarly, increasing the overlap percentage from 60% to 70% (S1 vs. S3) led to slightly more irregular surfaces, due to localised material accumulation. The deposition sequence also had a significant effect on the surface flatness in sample S4. When the edge was deposited before the infill (Edge-Infill), the surface showed the highest irregularity among the G1 group (0.35 mm). This result suggests that depositing the infill over a pre-existing edge perimeter may constrain melt pool accommodation, thereby compromising surface uniformity. Finally, rotating the layers by 90° in sample S5 led to intermediate roughness (0.29 mm), due to alternating thermal gradients between layers.

Table 5 provides a summary of the influence of the different process variables on the surface morphology, highlighting the key factors contributing to surface irregularity and waviness.

Table 5 Influence of process parameters on surface morphology

Process variable	Surface morphology response
Weaving	The absence of weaving leads to poorer molten pool redistribution, increasing surface height deviation and resulting in less uniform layer stacking.
Overlap percentage	Variations in overlap within the investigated range have a minor influence on surface quality. Higher overlap slightly increases surface irregularity due to localised material accumulation.
Deposition sequence	Depositing the edge prior to the infill constrains melt pool accommodation, producing the highest surface roughness and height deviation.
Infill strategy	Continuous linear infill paths (G2) promote uniform material distribution and yield the flattest surfaces, whereas concentric infill paths (G3) induce material buildup toward the centre, resulting in increased waviness.
Heat input	Surface morphology trends associated with the infill strategy remain consistent across different heat input levels, indicating that deposition path geometry plays a dominant role over heat input in governing surface waviness.

3.3 Microstructural characterisation

3.3.1 Phase evolution and cooling rates

Figure 10 shows the macrostructure and microstructure for the reference sample (S1), focusing on critical zones including the infill, the edge start and end positions (Fig. 10a) and the corner region (Fig. 10b). The cross-sections were extracted from the locations illustrated in Fig. 5a. Regions selected for microstructural characterisation are highlighted by white squares within the macrographs. The corresponding microstructural images are shown in Fig. 10c and e, representing the corner region (Fig. 10c), the edge start and end position (Fig. 10d), and the infill region (Fig. 10e), respectively.

In Fig. 10a and b, the cross-sections of the reference sample (S1) displays the characteristic layer-by-layer morphology of the deposited weld beads, with a uniform stacking pattern and well-defined bead interfaces, as well as a heat-affected zone (HAZ) in the substrate. The image highlights distinguishable microstructural regions corresponding to the edge and infill parameters. The microstructural analysis presented in Fig. 10c and e highlights the differences between the corner, edge and infill regions, showing how the thermal cycles and deposition parameters influence grain structure and phase distribution. In the edge and corner regions (Fig. 10c and d), the microstructure is characterised by larger grains, resulting from slower cooling rates due to the higher heat input and reduced heat dissipation in this area. This coarser structure consists of a mixture of phases, including bainite and acicular ferrite, the latter being distinguishable from the coexisting ferrite by its fine, interlocking needle-like morphology, in contrast to the coarser, equiaxed grains typical of ferrite. In contrast, the infill region (Fig. 10e) exhibits a more refined and uniform grain structure. This refinement is attributed to the faster cooling rates in the infill region, driven by lower heat input and enhanced heat dissipation facilitated by the surrounding deposited material. Similar to the edge region, the infill region also contains bainite and acicular ferrite, though with refined grain size.

To better understand the influence of the cooling rates on the microstructure, Fig. 11 shows micrographs from the infill region of the reference sample G1_C1_W_60_FE (Fig. 11a), sample G2_C1_W_60_FE (Fig. 11b) and edge region for the sample G1_C2_W_60_FE (Fig. 11c). These samples were selected to compare different printing strategies and heat inputs, directly affecting the Δt_{8-5} cooling times and resulting microstructures.

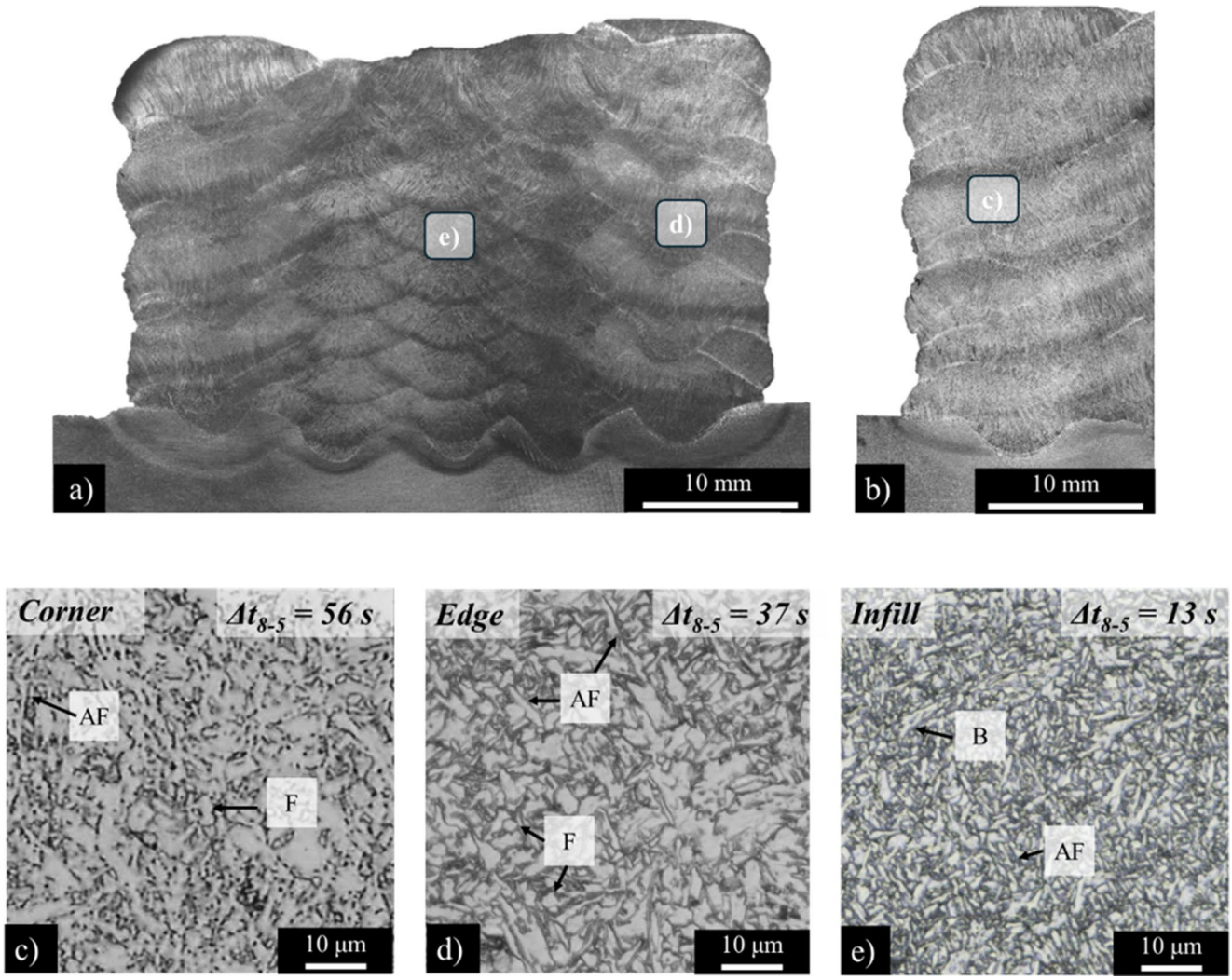

Fig. 10 Macrostructure and microstructure of the reference sample (S1): (**a** and **b**) cross-section of the sample, (**c**) microstructure of the corner region, (**d**) microstructure of the edge start and end positions and (**e**) microstructure of the infill region. Labels B, AF, and F indicate bainite, acicular ferrite, and ferrite, respectively

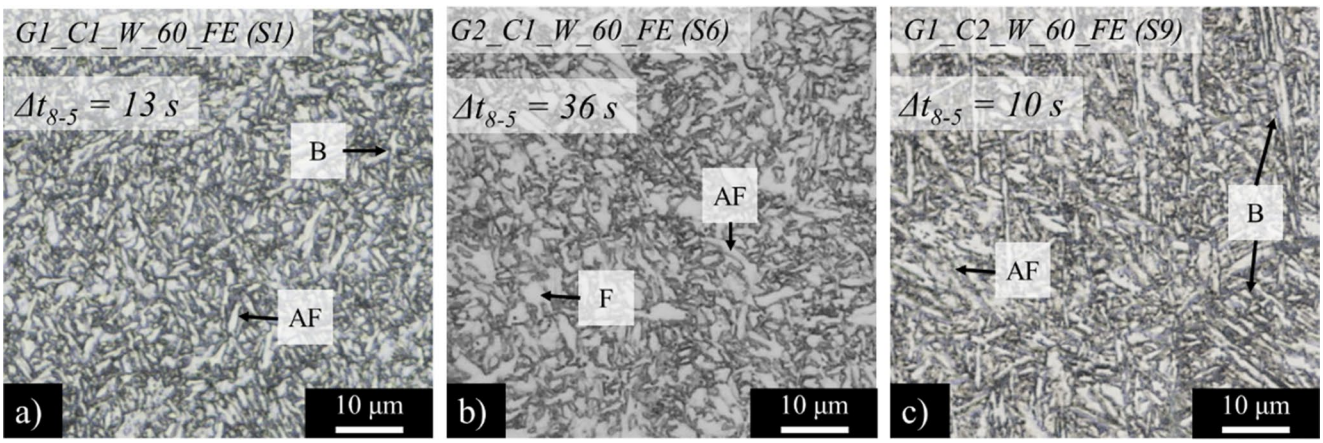

Fig. 11 Microstructure of the infill region for (**a**) reference sample G1_C1_W_60_FE (S1), with a Δt_{8-5} of 14 s, (**b**) sample G2_C1_W_60_FE (S6) with a Δt_{8-5} of 36 s and (**c**) sample G1_C2_W_60_FE (S9) with a Δt_{8-5} of 10 s. Labels B, AF, and F indicate bainite, acicular ferrite, and ferrite, respectively

Analysing the figure, it is possible to observe that the microstructure of sample G2_C1_W_60_FE (S6), produced using the G2 deposition strategy (Fig. 11b), exhibits a much coarser grain structure compared to the reference sample (Fig. 11a). The coarsening is attributed to the significantly higher cooling time, Δt_{8-5} of 36 s, resulting from the continuous, single-line infill deposition strategy employed in G2. Likewise, the microstructure of this sample resembles that of the edge region shown in Fig. 10b, which also had a Δt_{8-5} cooling time of around 36 s, further confirming the strong correlation between thermal cycles and microstructural evolution. Figure 11c shows the microstructure of sample G1_C2_W_60_FE (S9), produced using the G1 strategy with a higher travel speed and lower heat input (combination 2). This sample experienced the fastest cooling rate, with a Δt_{8-5} of 10 s, resulting in the most refined microstructure among the three samples. The rapid cooling inhibited grain growth, producing a highly refined bainitic grain structure.

This comparison demonstrates a precise coupling between the spatial thermal history and the resulting microstructure. The rapid cooling regime ($\Delta t_{8-5} \approx 10$ s), characteristic of the G1 strategy and Combination 2 parameters, effectively suppressed diffusion-controlled transformations, stabilising the refined bainitic and acicular ferrite matrix shown in Fig. 11a and c. Conversely, the high thermal accumulation ($\Delta t_{8-5} \approx 36$ s) inherent to the continuous G2 path provided the necessary time for diffusion, resulting in the coarsened ferrite structure observed in Fig. 11b. This establishes $\Delta t_{8-5} \approx 15$ s as a critical threshold in this alloy system for the transition between refined, hard transformation products and coarser ferritic structures.

3.3.2 Crystallographic orientation and grain structure

To further investigate the influence of infill deposition strategy (G1, G2, and G3) on microstructural evolution, EBSD analyses were performed on samples G1_C1_W_60_FE (S1), G2_C1_W_60_FE (S6), and G3_C1_W_60_EF (S7), all produced under the same processing conditions (Combination 1). As shown in Fig. 12, the EBSD scans were conducted in the infill region of each sample to enable a direct comparison of thermal effects associated with different path geometries.

The results reveal a clear trend of grain coarsening with the increased thermal accumulation, directly governed by the selected infill strategy. The G1 strategy (S1) produced the finest average grain size (2.39 µm), while the G2 (S6) and G3 (S7) strategies led to progressive grain growth, reaching 2.60 µm and 2.74 µm, respectively. This trend is further visualised in the grain size distribution histograms (Fig. 13a), where S1 displays a sharper peak at smaller diameters. This is accompanied by a steady decline in Kernel Average Misorientation (KAM) values, reflecting a reduction in local lattice strain and dislocation density, likely due to recovery or recrystallisation processes under prolonged thermal exposure. Sample S1 exhibited the highest average KAM (1.52°), indicating a high level of local misorientation and a dense network of geometrically necessary dislocations (GNDs), typical of a structure with limited thermal recovery. In contrast, samples S6 and S7, deposited using the G2 and G3 strategies under higher thermal accumulation, presented significantly lower average KAM values (0.92° and 0.93°, respectively). The KAM histograms (Fig. 13b) corroborate this, showing a distinct shift from a higher-angle distribution in S1 to a pronounced peak at low angles in S6 and S7. This reduction indicates a substantial decrease in internal lattice distortion, consistent with microstructural recovery or partial recrystallisation facilitated by extended thermal exposure and reduced cooling rates.

Grain boundary characterisation provides further insight into the microstructural evolution across the different deposition strategies. Low-angle grain boundaries (LAGBs), typically associated with sub grain structures and high dislocation densities, were predominant in S1 (G1 strategy), accounting for 73.7% of the total boundaries. This suggests a microstructure in an early stage of recovery, with significant residual deformation and limited recrystallisation. In contrast, samples S6 (G2 strategy) and S7 (G3 strategy) exhibited a significant reduction in LAGBs (~53%) and an increase in high-angle grain boundaries (HAGBs) to 46%. The presence of HAGBs, which are indicative of newly formed, strain-free grains, points to advanced recovery and recrystallisation driven by thermal accumulation during deposition. Overall, the results demonstrate that heat input and deposition strategy govern the cooling rate and thermal accumulation, which in turn control grain coarsening, recovery, and recrystallisation mechanisms in WAAM-fabricated thick-walled components.

3.4 Defect analysis and quality assessment

This section provides a comprehensive analysis of the defects identified in the fabricated components, focusing on their types, spatial distribution, and correlation with process parameters. Figure 14 illustrates higher magnifications of the primary defect types encountered, including pores, lack of fusion, overlap, and voids. Additionally, the spatial distribution and locations of these defects across the cross-sections of the samples are detailed in Fig. 15, with defects colour-coded for clarity. Figure 15 also displays the macrostructure of the cross-section for all fabricated samples, systematically organised to assess the influence of different deposition strategies and parameters. The columns represent the effect of the infill deposition strategy

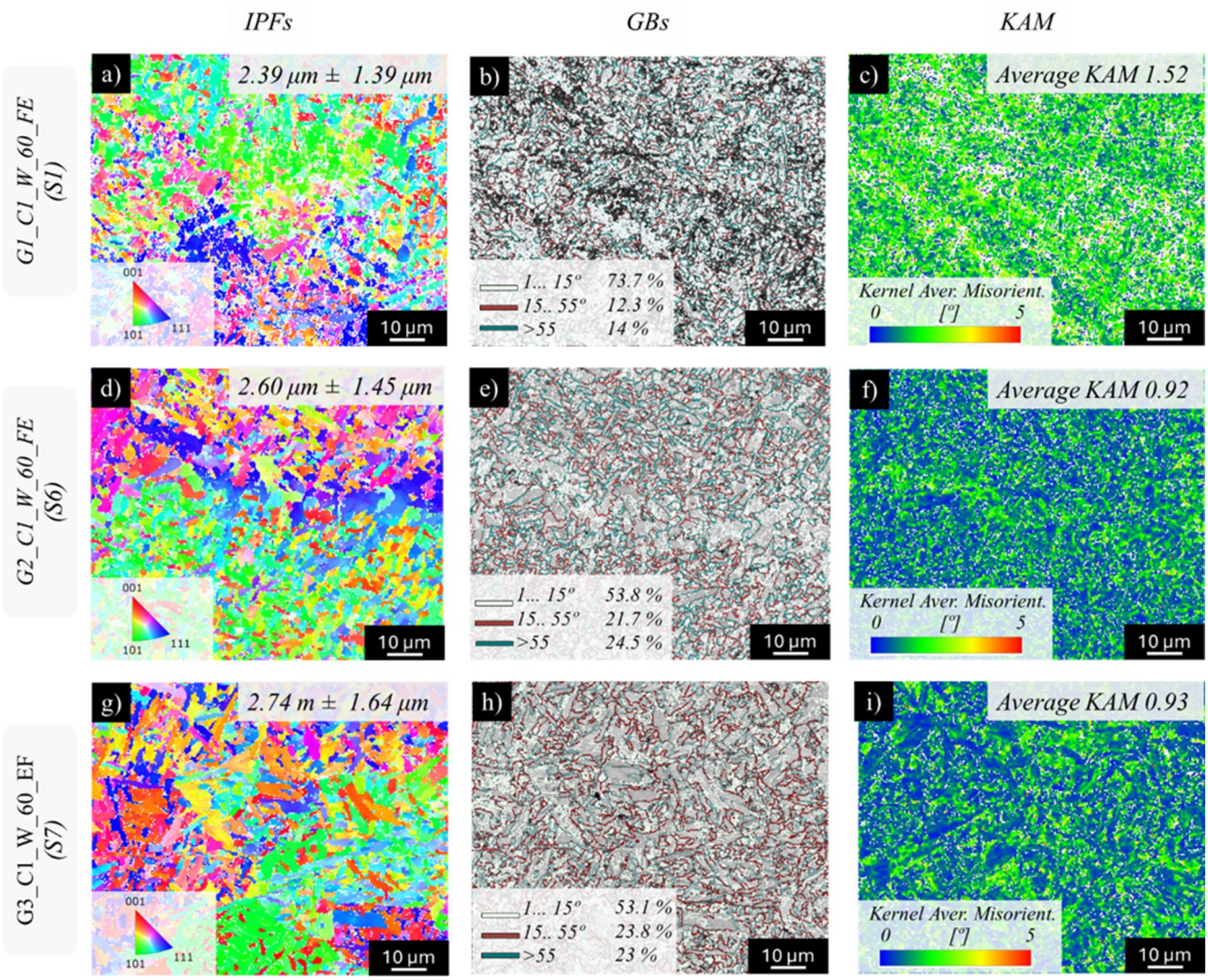

Fig. 12 EBSD characterisation of the infill region for samples G1_C1_W_60_FE (**a**–**c**), G2_C1_W_60_FE (**d**–**f**), and G3_C1_W_60_EF (**g**–**i**). Subfigures show: (**a**, **d**, **g**) grain size distribution maps with quantitative grain size analysis; (**b**, **e**, **h**) grain boundary maps distinguishing high-angle and low-angle grain boundaries; and (**c**, **f**, **i**) Kernel Average Misorientation (KAM) maps illustrating local misorientation and strain distribution for each sample

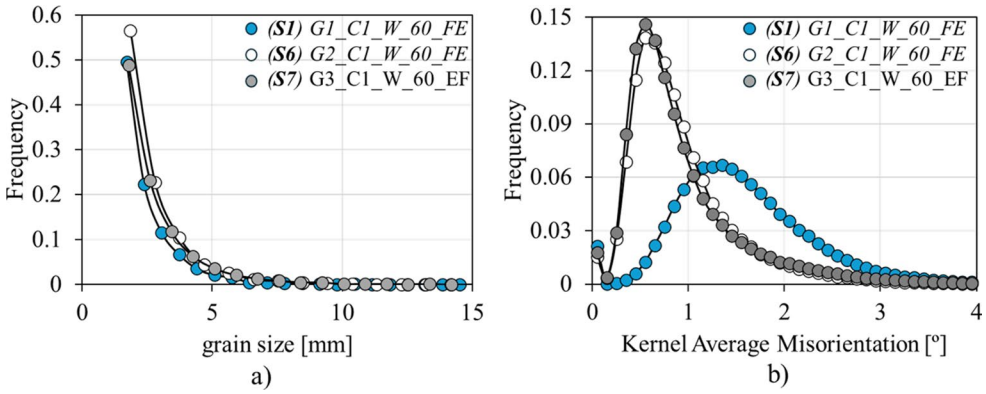

Fig. 13 (**a**) Grain size distribution histograms and (**b**) kernel average misorientation histograms for the G1_C1_W_60_FE (S1), G2_C1_W_60_FE (S6), and G3_C1_W_60_EF (S7) samples

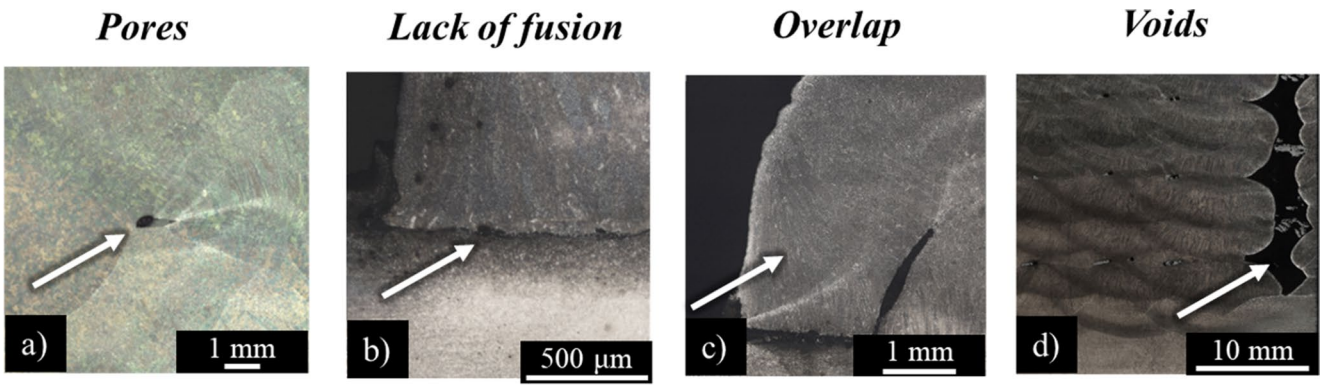

Fig. 14 Examples of defects observed in WAAM-fabricated components such as (**a**) pores, (**b**) lack of fusion, (**c**) overlap and (**d**) voids. Scale bars are provided for reference, highlighting the size and morphology of the defects observed in the metallographic samples

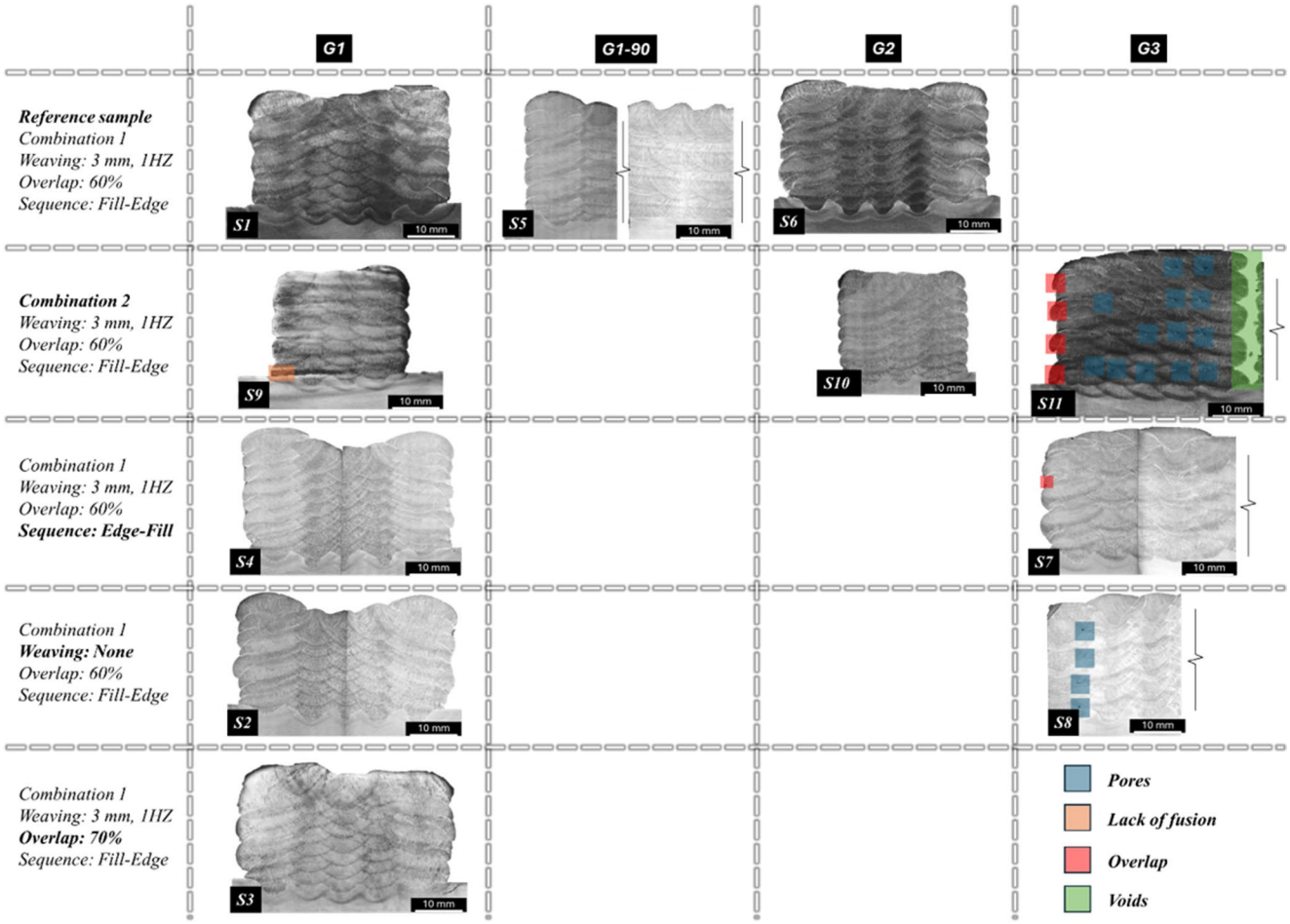

Fig. 15 Distribution of defects in all produced samples: pores, lack of fusion, overlap and voids

(G1, G1-90, G2, and G3), while the rows capture the impact of heat input (second row), production sequence (third row), weaving (fourth row), and overlap strategy (fifth row). For samples with a square morphology (G1-90 and G3), only a partial cross-sectional area is shown due to the large sample size.

Large pores were prominently identified in samples S8 and S11, manufactured using the G3 deposition strategy, which exhibited a higher propensity for defect formation, particularly at the interface between different layers. This issue was especially pronounced in S8, where the absence of weaving led to inefficient distribution of the molten pool

across the previously deposited material. In S11, more pore defects were also observed, attributed to the combination of the G3 strategy and lower heat input process parameters. Additionally, S11 exhibited a large void at its centre, caused by the insufficient flowability of the molten pool under low heat input conditions, which hindered complete material filling within the internal region of the sample. Despite the registered defects for S8 and S11, these are avoidable by further optimisation of the deposition strategy, such as overlap and travel speed. The lack of fusion defects were observed in sample S9, produced with low heat input process parameters. This defect was observed particularly in the edge weld bead, at the deposition starting position, where inadequate energy input led to insufficient bonding between the deposited material and the substrate. Finally, overlap defects were also observed in sample S11. This defect is characterised by an excess of molten metal flowing over the surface of the base material without properly fusing it. This results in an additional layer or bead of metal sitting on top of the base material rather than being properly fused into it.

The results highlighted the need to balance heat input, weaving, and deposition strategy to minimise defect formation in WAAM. Weaving is particularly effective in promoting material distribution, while careful control of heat input and selection of deposition strategies are essential to prevent defects such as lack of fusion, voids, and overlaps.

Table 6 summarises the results from the radiographic analysis conducted on the fabricated samples. The inspection was carried out according to the acceptance criteria specified in EN ISO 10675-1:2021 (Level 1) [38]. The results indicate that all samples, except for G3_C1_N_60_EF (S8 sample), were in good condition with no detectable defects. In the case of sample G3_C1_N_60_EF, solid inclusions were identified, categorising it as "Acceptable" under the standard guidelines. For future components where defects might exceed these thresholds, standard repair procedures are recommended. These typically involve the mechanical removal of the defective area through grinding or milling, followed by localised re-deposition to restore the structural integrity of the component.

The radiographic analysis, while useful for identifying macroscopic defects like solid inclusions, highlights its limitations in providing detailed insights into the underlying mechanisms of defect formation and smaller-scale imperfections. For instance, while the radiographic analysis confirmed the presence of solid inclusions, it could not capture other critical defects, such as lack of fusion, voids, or overlap issues identified in the metallographic examination. The radiographic findings further emphasise the importance of combining different inspection methods to achieve a more holistic understanding of defect formation in WAAM-fabricated components.

To synthesise the findings regarding defect formation, Table 7 summarises the main defect types observed, the specific strategies affected, and the primary physical causes identified.

Table 6 – Radiographic results, according to EN ISO 10675-1:2021 [38]

Sample ID	Nomenclature	Acceptance	Note
S1	G1_C1_W_60_FE	–	
S2	G1_C1_N_60_FE	–	
S3	G1_C1_W_70_FE	–	
S4	G1_C1_W_60_EF	–	
S5	G1-90_C1_W_60_FE	–	
S6	G2_C1_W_60_FE	–	
S7	G3_C1_W_60_EF	–	
S8	G3_C1_N_60_EF	/	Solid inclusion
S9	G1_C2_W_60_FE	–	
S10	G2_C2_W_60_FE	–	
S11	G3_C2_W_60_EF	–	

No Significant Defect (NSD) – Acceptable / Repair +

3.5 Mechanical characterisation

The presence of a heterogeneous microstructure along the building direction of the produced solids was also analysed through hardness measurements. To assess the variation in mechanical properties along the building direction, vertical microhardness profiles were measured for both the edge, corner and infill regions of reference sample G1_C1_W_60_FE (S1). Figure 16 presents these measurements, with Fig. 16a showing the evolution of hardness along the build direction for the edge (red lines), corner (green) and infill (blue lines) regions, and Fig. 16b and c provide a detailed hardness distribution map across the samples cross-section. The figure shows that hardness

Table 7 – Summary of defect types, governing parameters, and formation mechanisms

Defect type	Dominant conditions	Governing mechanism
Porosity	Concentric infill strategy (G3), low heat input, absence of weaving	Restricted melt pool spreading and reduced gas escape due to confined deposition paths and insufficient energy input.
Void formation	Concentric infill strategy (G3) combined with low heat input	Insufficient molten material flow toward the centre of the component, preventing complete filling during solidification.
Lack of fusion	Low heat input, bead start locations	Inadequate remelting of the underlying material during arc initiation, leading to incomplete metallurgical bonding.
Overlap defects	Localised regions in concentric infill samples	Molten metal flowed over the base material without fusing, caused by the unstable arc dynamics and thermal saturation at the concentric path.

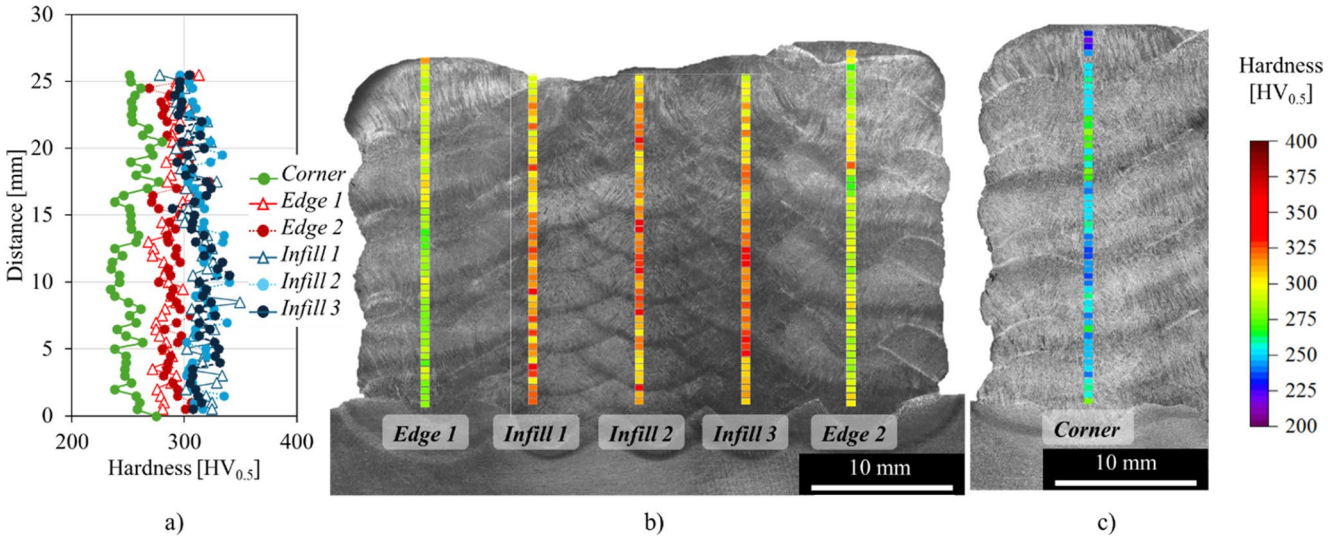

Fig. 16 Microhardness profiles and hardness distribution map for the G1_C1_W_60_FE (S1) sample: (**a**) hardness profiles along the build direction for edge regions (red profiles), corner (green profiles) and infill regions (blue profiles); (**b** and **c**) hardness distribution map across the sample cross-section

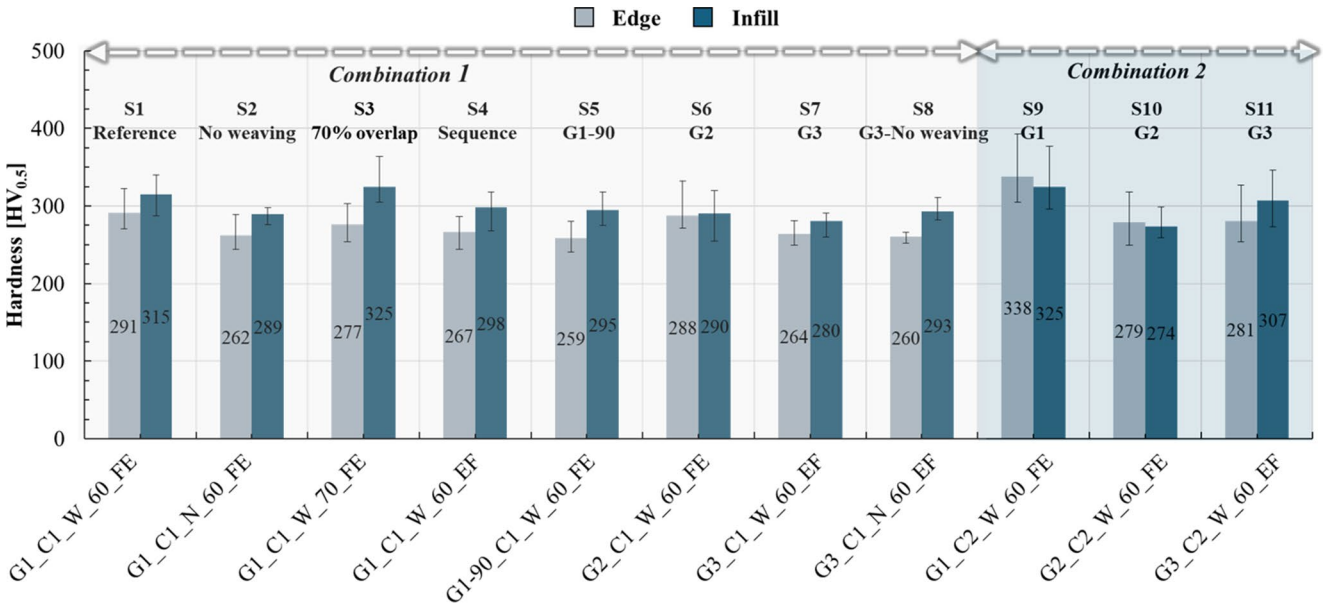

Fig. 17 Average hardness values for the edge and infill regions of all produced samples, with error bars representing the range of maximum and minimum hardness values

values were consistently higher in the infill regions than in the edge and corner regions. This discrepancy resulted from the lower heat input parameter used for the infill, which promoted faster cooling rates and a more refined microstructure, thereby increasing the hardness values. In contrast, the edge regions, deposited with higher heat input, had lower hardness values. The corner region displayed the lowest hardness values among all zones, in agreement with the highest Δt_{8-5} cooling time observed in this area (Fig. 6). The prolonged thermal exposure in the corners facilitated significant grain growth and suppressed the formation of hard transformation phases, thereby reducing local hardness.

To highlight how the deposition parameters and strategies influenced the hardness values across the produced samples, Fig. 17 shows the average hardness values for all samples in the edge and infill regions, with error bars indicating the range between the maximum and minimum hardness values registered in each region for each sample. Despite using various printing strategies and process parameters, the average hardness values exhibit only moderate variation, suggesting uniform mechanical

properties across all samples. Nevertheless, distinct trends may be observed when comparing the edge and infill regions for the two parameter combinations. For samples fabricated with combination 1, the hardness values are consistently higher in the infill regions compared to the edges. This trend reflects the faster cooling rates and finer microstructures achieved in the infill due to the lower heat input used in this region. Conversely, for combination 2, the edge regions exhibit higher average hardness values than the infill. This is attributed to the higher heat input applied to the infill in Combination 2, which resulted in slower cooling rates and coarser microstructures, ultimately reducing hardness in the infill.

Also, while the G2 printing strategy produced coarser microstructures in the infill regions for combination 1, the hardness values remained relatively unaffected compared to the other strategies in the same combination. On the other hand, for combination 2 parameters, the differences in hardness values between strategies become more pronounced. Among the samples produced with combination 2, the G1 strategy produced the highest hardness values, followed by G3, while G2 exhibited the lowest hardness values.

To better understand these results, Fig. 18 shows the evolution of the average hardness values and the Δt_{8-5} cooling times for the edge and infill regions across all samples, as previously calculated in Fig. 7. The figure also includes a trend line (black dashed line) representing the overall correlation and a green shaded area indicating the standard deviation, determined from the average hardness values measured for all samples. The figure shows an inverse relationship between hardness and Δt_{8-5}, more pronounced for lower cooling times. Hardness values exhibit higher variation for Δt_{8-5} below 12 s. This trend was particularly pronounced for the samples produced with combination 2, where the lower heat input parameters led to faster cooling rates and more noticeable hardness variations. In contrast, for samples produced with combination 1, where Δt_{8-5} values exceeded 12 s, the hardness values showed a more gradual decrease with the increase of the cooling time. The slower cooling rates under these conditions result in a reduced variation in the hardness values. This trend explains why the differences in hardness were less pronounced in Fig. 17, for the samples produced with combination 1, as the average and standard deviation values overlapped, masking the influence of Δt_{8-5}.

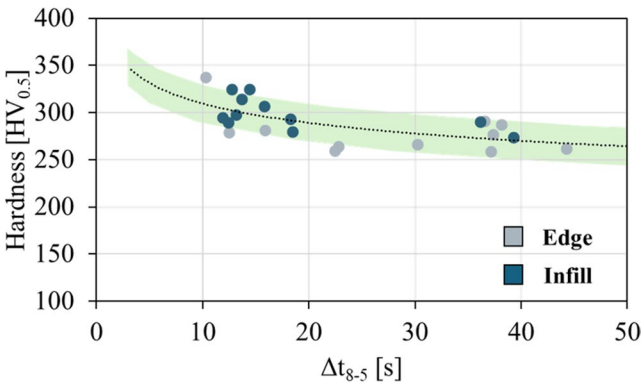

Fig. 18 Evolution of the hardness values with the Δt_{8-5} cooling times for edge and infill regions for all samples produced. The black dashed line represents the overall trend, while the shaded area indicates the standard deviation of hardness values

These findings are consistent with the EBSD results, where samples subjected to lower Δt_{8-5} values exhibited finer grains, higher local misorientation and a higher proportion of low-angle grain boundaries, features typically associated with increased hardness.

4 Conclusions

In this work, several printing strategies were used to produce thick steel components, evaluating their influence on the thermal cycles, production rates, microstructure, defect formation and hardness. The main conclusions reached were:

- During the manufacturing of WAAM components, the thermal cycles observed were predominantly governed by the heat input, with the deposition sequence playing a secondary role. Strategies such as weaving and overlapping percentage variations had minimal influence within the tested parameter ranges. However, the analysis revealed that corner regions are critical zones for heat accumulation, with cooling times in these areas potentially reaching three times the duration observed for the straight deposition paths.
- Surface morphology analysis using laser profilometry demonstrated that all deposition strategies produced first-layer standard deviations below 1 mm. However, the continuous linear strategy consistently yielded the flattest surfaces due to its uninterrupted path, while the concentric deposition strategy, characterised by centralised start/stop positions, led to the highest surface waviness. Additionally, within the linear parallel alternating strategy, minor changes such as weaving, overlap percentage, and deposition sequence significantly affected surface uniformity, with the absence of weaving and edge-first sequences notably increasing surface waviness.
- The concentric printing strategy demonstrated the highest susceptibility to defect formation, particularly pores and voids concentrated at layer interfaces. Samples produced without weaving presented more pores and voids,

highlighting the crucial role of weaving in ensuring effective material distribution and mitigating defect formation. Furthermore, lower heat input parameters lead to lack of fusion defects, especially at bead starting positions, where minimal heat accumulation is observed. Also, metallographic analysis provided deeper insights into the defect formation mechanisms compared to radiographic techniques.

- Mechanical properties were influenced by thermal cycles, with faster cooling rates resulting in finer microstructures and higher hardness values. Despite varying printing strategies, the hardness differences across samples were limited for faster cooling rates, where $\Delta t_{8\text{-}5}$ was less than 12 s.

Author contribution David Andrade: Visualization, Formal analysis, Investigation, Writing - Original Draft, Writing - Review & Editing; Carlos Zhu: Investigation, Formal analysis, Methodology, Writing - Review & Editing; Hagar El Bamby: Investigation, Formal analysis, Visualisation; Kaike Pinto Monteiro: Investigation; Sree Sabari: Investigation, Writing - Review & Editing; Luís Simões da Silva: Supervision, Writing - Review & Editing; Ramesh Babu: Formal analysis, Writing - Review & Editing; Trayana Tankova: Conceptualization, Methodology, Formal analysis, Supervision, Writing - Review & Editing, Funding Acquisition.

Funding This work has received funding from:
- The Research Fund for Coal and Steel under grant agreement 101112614 — IAMFat.
-This work was partly financed by FCT / MCTES through national funds (PIDDAC) under the R&D Unit Institute for Sustainability and Innovation in Structural Engineering (ISISE), under reference UIDB / 04029/2020 (https://doi.org/10.54499/UIDB/04029/2020), and under the Associate Laboratory Advanced Production and Intelligent Systems ARISE under reference LA/P/0112/2020.
-This work was partly funded by national funds through FCT – Foundation for Science and Technology, under grant agreement 2021.05992.BD attributed to C. Zhu.
- This work was partly funded by national funds through FCT – Foundation for Science and Technology, under grant agreement 2022.11969 attributed to K. Monteiro.

Declarations

Competing interest The authors declare that they have no known competing financial interests or personal relationships that could have appeared to influence the work reported in this paper.

References

1. Sanaei N, Fatemi A (2021) Defects in additive manufactured metals and their effect on fatigue performance: A state-of-the-art review. Prog Mater Sci 117:100724. https://doi.org/10.1016/j.pmatsci.2020.100724
2. 10025-1:2004 BE (n.d) Hot-rolled products of structural steels-Part1: General technical delivery conditions
3. Rodrigues TA, Duarte V, Miranda RM, Santos TG, Oliveira JP (2019) Current status and perspectives on wire and arc additive manufacturing (WAAM). Materials (Basel) 12. https://doi.org/10.3390/ma12071121
4. Treutler K, Wesling V (2021) The current state of research of wire arc additive manufacturing (Waam): a review. Appl Sci 11. https://doi.org/10.3390/app11188619
5. Çam G, Günen A (2024) Challenges and opportunities in the production of magnesium parts by directed energy deposition processes. J Magnes Alloy 12:1663–1686. https://doi.org/10.1016/j.jma.2024.05.004
6. Palmeira Belotti L, van Dommelen JAW, Geers MGD, Goulas C, Ya W, Hoefnagels JPM (2022) Microstructural characterisation of thick-walled wire arc additively manufactured stainless steel. J Mater Process Technol 299. https://doi.org/10.1016/j.jmatprotec.2021.117373
7. Wang C, Liu TG, Zhu P, Lu YH, Shoji T (2020) Study on microstructure and tensile properties of 316L stainless steel fabricated by CMT wire and arc additive manufacturing. Mater Sci Eng A 796. https://doi.org/10.1016/j.msea.2020.140006
8. Wang C, Lu YH, Zhu P, Shoji T (2023) *In-situ* observation of deformation behavior of the periodic structure in 316L stainless steel fabricated by wire and arc additive manufacturing. Mater Charact 203. https://doi.org/10.1016/j.matchar.2023.113162
9. Andrade DG, Tankova T, Zhu C, Branco R, Simões da L, Rodrigues DM (2024) Mechanical properties of 3D printed CMT-WAAM 316 LSi stainless steel walls 215. https://doi.org/10.1016/j.jcsr.2024.108527
10. Laghi V, Arrè L, Tonelli L, Di Egidio G, Ceschini L, Monzón I et al (2023) Mechanical and microstructural features of wire-and-arc additively manufactured carbon steel thick plates. Int J Adv Manuf Technol 127:1391–1405. https://doi.org/10.1007/s00170-023-11538-3
11. Tankova T, Andrade D, Branco R, Zhu C, Rodrigues D, Simões da Silva L (2022) Characterization of robotized CMT-WAAM carbon steel. J Constr Steel Res 199. https://doi.org/10.1016/j.jcsr.2022.107624
12. Liu J, Xu Y, Ge Y, Hou Z, Chen S (2020) Wire and arc additive manufacturing of metal components: a review of recent research developments. Int J Adv Manuf Technol 111:149–198. https://doi.org/10.1007/s00170-020-05966-8
13. Jafari D, Vaneker THJ, Gibson I (2021) Wire and arc additive manufacturing: Opportunities and challenges to control the quality and accuracy of manufactured parts. Mater Des 202:109471. https://doi.org/10.1016/j.matdes.2021.109471
14. Zhang J, Xing Y, Cao J, Zhang X, Yang F (2022) The gap-filling overlapping model for wire and arc additive manufacturing of multi-bead components. Int J Adv Manuf Technol 123:737–748. https://doi.org/10.1007/s00170-022-10132-3
15. Ding D, Yuan L, Huang R, Jiang Y, Wang X, Pan Z (2023) Corner path optimization strategy for wire arc additive manufacturing of gap-free shapes. J Manuf Process 85:683–694. https://doi.org/10.1016/j.jmapro.2022.12.014
16. Palmeira Belotti L, van Dommelen JAW, Geers MGD, Ya W, Hoefnagels JPM (2024) Influence of the printing strategy on the microstructure and mechanical properties of thick-walled wire

arc additive manufactured stainless steels. J Mater Process Technol 324. https://doi.org/10.1016/j.jmatprotec.2023.118275
17. Tiwari Y, Nandi S, Manivannan R, Chatterjee D, Mukherjee M, Rajinikanth V (2024) Investigating the influence of various tool path trajectories on the anisotropic behaviour of bulk NiCrMo-3 alloy fabrication by WADED process. Mater Charact 209:113742. https://doi.org/10.1016/j.matchar.2024.113742
18. Li Y, Han Q, Zhang G, Horváth I (2018) A layers-overlapping strategy for robotic wire and arc additive manufacturing of multi-layer multi-bead components with homogeneous layers. Int J Adv Manuf Technol 96:3331–3344. https://doi.org/10.1007/s00170-018-1786-3
19. Müller J, Hensel J (2023) WAAM of structural components—building strategies for varying wall thicknesses. Weld World 67:833–844. https://doi.org/10.1007/s40194-023-01481-y
20. Suryakumar S, Karunakaran KP, Bernard A, Chandrasekhar U, Raghavender N, Sharma D (2011) Weld bead modeling and process optimization in Hybrid Layered Manufacturing. CAD Comput Aided Des 43:331–344. https://doi.org/10.1016/j.cad.2011.01.006
21. Chen C, He H, Zhou J, Lian G, Huang X, Feng M (2022) A profile transformation based recursive multi-bead overlapping model for robotic wire and arc additive manufacturing (WAAM). J Manuf Process 84:886–901. https://doi.org/10.1016/j.jmapro.2022.10.042
22. Ding D, Pan Z, Cuiuri D, Li H (2015) A multi-bead overlapping model for robotic wire and arc additive manufacturing (WAAM). Robot Comput Integr Manuf 31:101–110. https://doi.org/10.1016/j.rcim.2014.08.008
23. Li Y, Sun Y, Han Q, Zhang G, Horváth I (2018) Enhanced beads overlapping model for wire and arc additive manufacturing of multi-layer multi-bead metallic parts. J Mater Process Technol 252:838–848. https://doi.org/10.1016/j.jmatprotec.2017.10.017
24. Banaee SA, Kapil A, Marefat F, Sharma A (2023) Generalised overlapping model for multi-material wire arc additive manufacturing (WAAM). Virtual Phys Prototyp 18. https://doi.org/10.1080/17452759.2023.2210541
25. Iqbal H, Ascari A, Liverani E, Fortunato A (2025) Analysis of process parameters, deposition strategies and build orientations in wire-arc additive manufacturing (WAAM). Prog Addit Manuf 10:5711–5729. https://doi.org/10.1007/s40964-024-00938-w
26. Li Y, Shi C, Wang X, Yuan S, Zhu J, Zhang W (2025) A mapping-based graded infill structure design method and continuous printing path planning. Addit Manuf 98:104639. https://doi.org/10.1016/j.addma.2025.104639
27. Köhler M, Sun L, Hensel J, Pallaspuro S, Kömi J, Dilger K et al (2021) Comparative study of deposition patterns for DED-Arc additive manufacturing of Al-4046. Mater Des 210. https://doi.org/10.1016/j.matdes.2021.110122
28. Tankova T, Zhu C, El Bamby H, Monteiro K, Sabari S, da Silva LS et al (2026) Influence of metal transfer modes and process conditions on WAAM-fabricated AM46 carbon steel walls. Structures, vol 84. Elsevier, vol 84p 110936
29. 10025-6:2019+A 1:2022 BE. Hot rolled products of structural steels - part 6: technical delivery conditions for flat products of high yield strength structural steels in the quenched and tempered condition 2022
30. Queguineur A, Asadi R, Ostolaza M, Valente EH, Nadimpalli VK, Mohanty G et al (2023) Wire arc additive manufacturing of thin and thick walls made of duplex stainless steel. Int J Adv Manuf Technol 127:381–400. https://doi.org/10.1007/s00170-023-11560-5
31. Hu Z, Qin X, Li Y, Yuan J, Wu Q (2020) Multi-bead overlapping model with varying cross-section profile for robotic GMAW-based additive manufacturing. J Intell Manuf 31:1133–1147. https://doi.org/10.1007/s10845-019-01501-z
32. Welding BSI BS EN 1011-1:2009. Welding — recommendations for welding of metallic materials. Part 1: general guidance for arc welding 2001
33. Andrade DG, Zhu C, Miranda HC, Rodrigues DM (2024) Thermal, Microstructural, and Mechanical Analysis of Complex Lattice Structures Produced by Direct Energy Deposition. Mater (Basel). https://doi.org/10.3390/ma17122813
34. Zhu C, Tankova T, Azar AS, Branco R, da Silva LS (2025) Framework for automated measurement of material deposition in welding and directed energy deposition. Int J Adv Manuf Technol 140:1625–1644. https://doi.org/10.1007/s00170-025-16354-5
35. ASTM. ASTM E3-11 (2017) Standard guide for preparation of metallographic specimens 2017
36. ISO ISO 17636-1:2022. Non-destructive testing of welds — radiographic testing — part 1: X- and gamma-ray techniques with film 2022
37. Easterling K (2013) Introduction to the physical metallurgy of welding. Elsevier
38. ISO ISO 10675-1:2021. Non-destructive testing of welds — acceptance levels for radiographic testing — part 1: steel, nickel, titanium and their alloys 2021